MTLA 46 (2026) 102748

Contents lists available at ScienceDirect

Materialia

journal homepage: www.elsevier.com/locate/mtla

Full Length Article

3D printed multi-material scaffolds: integrating bioceramic with metal for enhanced bone scaffold performance

S. Panahkhahi [a,b,*], M.H. Zwart [a], V. Moosabeiki [a], L.B. Kunkels [a], M.A. Leeflang [a], M. Klimopoulou [a], N.E. Putra [a], L.E. Fratila-Apachitei [a], J. Zhou [a], M.J. Mirzaali [a,*,1], A.A. Zadpoor [a,1]

[a] Department of Biomechanical Engineering, Faculty of Mechanical Engineering, Delft University of Technology, Mekelweg 2, 2628 CD, Delft, The Netherlands
[b] Research Group Technology for Healthcare, Centre of Expertise Health Innovation, The Hague University of Applied Science, Rotterdamseweg 137, 2628 AL, Delft, The Netherlands

ARTICLE INFO

Keywords:
Direct ink writing
Multi-material 3D printing
Multi-functional bone scaffold
Bone tissue repair
Tissue engineering

ABSTRACT

This study was the first attempt to design, fabricate, and evaluate multi-material bone scaffolds composed of Ti6Al4V and akermanite ($Ca_2Mg(Si_2O_7)$, Ak), produced *via* direct ink writing (DIW), followed by sintering. Two scaffold architectures were developed (i.e., monolithic and core-shell) aimed at combining the mechanical strength of the Ti alloy with the osteoinductive properties of Ak. Uniaxial compression testing demonstrated that the core-shell scaffolds exhibited higher relative-density-normalized elastic moduli (up to 7.65 ± 0.35 GPa) and yield strengths (up to 444.7 ± 8.1 MPa) than the monolithic designs, namely Ti6Al4V-only scaffolds (elastic modulus: 4.29 ± 0.18 GPa; yield strength: 230.9 ± 1.7 MPa) and 90% Ti6Al4V/10% Ak composite scaffolds (elastic modulus: 3.05 ± 0.08 GPa; yield strength: 24.7 ± 1.4 MPa).The enhanced mechanical performance was attributed to interfacial reinforcement and optimized material distribution. Bioactivity assays in r-SBF revealed surface Ca–P deposition on akermanite-containing scaffolds by SEM and EDS, a response not observed on Ti6Al4V only specimens. Complementary ICP-OES showed marked depletion of phosphate and calcium ions, consistent with rapid HAp nucleation and growth, and substantial silicon release in composite samples, a known pro-osteogenic stimulus. Cell culture assays further confirmed the cytocompatibility of the Ti6Al4V, composite and core-shell scaffolds for preosteoblasts. Furthermore, SEM imaging showed that all the scaffolds supported cell attachment and evidenced a distinct cell spatial distribution depending on scaffold composition and architecture. These results contribute to advancing the scaffold design for bone repair and regeneration by proposing DIW-fabricated Ti6Al7V/Ak core-shell scaffolds that show potential as customizable, load-bearing implants with improved mechanical properties and surface bioactivity relative to the Ti6Al4V scaffolds.

1. Introduction

Large bone defects, resulting from musculoskeletal tumors, infections, or trauma, present a significant clinical challenge, as these defects often exceed the body's intrinsic regenerative capacity and require surgical intervention [1]. Current treatment strategies rely heavily on bone grafts, including autografts, allografts, and synthetic substitutes. Among these, autografts are considered the gold standard due to their perfect histocompatibility and superior regenerative outcomes [2]. However, they are constrained by limited availability and donor site morbidity, which can lead to additional patient discomfort and complications [3]. Allografts offer an alternative but are associated with the risks of immune rejection and variable integration due to reduced histocompatibility [1]. Despite these drawbacks, over two million bone graft procedures, mostly relying on these bone grafts, are performed annually worldwide, highlighting the pressing need for more effective and accessible bone repair and regeneration solutions [4,5].

Synthetic bone grafts and orthopedic implants have in recent years emerged as a promising alternative, aiming to replicate the mechanical and biological functionalities of the native bone. Metallic biomaterials, such as Ti6Al4V, are frequently used due to their excellent strength, biocompatibility, and corrosion resistance [6]. Titanium is a

* Corresponding authors.
E-mail addresses: S.Panahkhahi@tudelft.nl (S. Panahkhahi), M.J.Mirzaali@tudelft.nl (M.J. Mirzaali).
[1] These authors supervised this work equally.

https://doi.org/10.1016/j.mtla.2026.102748
Received 31 March 2026; Accepted 14 April 2026
Available online 15 April 2026

paramagnetic material, making it compatible with MRI procedures due to minimal risks of implant displacement or heating. Although Ti and its alloys may cause localized imaging artifacts, due to the interactions with the magnetic field, these artifacts can be effectively minimized using advanced imaging techniques [7]. Despite its excellent mechanical properties, Ti is inherently bioinert and lacks osteoinductive properties, which can hinder bone regeneration and potentially lead to long-term implant failure [1]. To overcome these limitations, various surface modification strategies, particularly those involving functional coatings, have been developed to enhance the biological performance of Ti-based implants ([8,9],). However, strong adhesion of coating to the Ti substrate is often hard to achieve, leading to delamination during implant insertion or under physiological loading, and cracking often occurs due to different mechanical and physical properties of the coating from those of the Ti substrate. Moreover, achieving homogeneous coating on the surfaces of geometrically complex substrates, typically of bone scaffolds with high porosity, is technically challenging [10]. Uneven coating thickness may create corrosion pathways and increase susceptibility to bacterial infiltration ([11,12],).

To avoid the shortcomings inherent to the coating strategy, in this study we adopted an alternative approach by creating architected, hierarchical metal–bioceramic composites. We selected the biocompatible Ti alloy (Ti-6Al-4 V) for its mechanical strength and a bioactive ceramic for its osteogenic potential to form Ti-matrix composites, with the aim of enhancing scaffold biocompatibility while preserving the mechanical performance required for load-bearing applications. Leveraging multimaterial printing, we incorporate bioceramic phases in spatially controlled regions to promote osteogenic response and bone formation within a mechanically stable scaffold, thereby addressing the individual limitations associated with bioinert metallic scaffolds and with brittle bioceramic scaffolds. Bioactive inorganic materials—spanning both ceramics and glasses—have in recent years attracted considerable attention due to their greater capacity to promote osteogenesis and modulate immune responses ([13,14],) than more common calcium phosphate (CaP) ceramics. Within the bioactive glass family, 45S5 Bioglass is a prominent and highly bioactive composition; however, it exhibits a pronounced tendency to crystallize during heat treatment, which can inhibit sintering and complicate the fabrication of mechanically reliable porous scaffolds [15].

Notably, akermanite ($Ca_2Mg(Si_2O_7)$, Ak), demonstrates a strong apatite-forming capability when immersed in simulated body fluid (SBF), resulting in the rapid formation of a bone-like apatite layer on its surface. This layer significantly enhances the scaffold's bioactivity by fostering robust bonding with native bone tissue, thereby accelerating osseointegration [16].

However, the intrinsic brittleness of bioceramics, including akermanite, restricts their application in load-bearing context. Consequently, there is a strong need to develop composite scaffolds that integrate the mechanical strength of metals with the biological functionality of bioceramics to enable effective bone regeneration.

Among the additive manufacturing (AM) techniques that are capable of producing multi-material highly porous scaffolds, direct ink writing (DIW) stands out, as it enables precise deposition of multi-material inks to create architecturally complex, functionally graded scaffolds [17]. This 3D printing technique uniquely allows for the spatially controlled incorporation of a bioceramic within a metal matrix, thus offering significant advantages over conventional surface coating methods that often suffer from limited compositional tunability and lack structural continuity ([11,12],). To enhance scaffold performance, engineered porosity and hierarchical architectures are both necessary. Controlled porosity not only tailors the stiffness of the scaffold to match that of the cortical bone, thereby reducing stress shielding, but also facilitates vascularization, nutrient diffusion, and bone tissue in-growth ([18–20]). According to the Gibson and Ashby model, mechanical properties, such as elastic modulus and yield strength, can be effectively tuned by varying scaffold density and unit cell geometry [21,22]. Guided by this model, we designed two distinct scaffold architectures. (i) A lattice architecture featuring 400 μm strut spacing with alternating 0°/90° layers, fabricated using either Ti-6Al-4 V ink or a Ti-6Al-4V–Akermanite composite (TiAk) ink (Fig. 1a). However, when Akermanite was incorporated by a homogeneous mixing approach in this first design, the resulting TiAk lattices did not exhibit satisfactory mechanical performance and showed pronounced brittleness (Fig. 3j). (ii) To address this limitation and to systematically investigate the influence of architectural partitioning on mechanical response, we developed a core–shell (CS) scaffold architecture in which either a Ti-6Al-4 V core is encased by a TiAk shell or, conversely, a TiAk core is encased by a Ti-6Al-4 V shell. Inspired by the structural organization of the femoral midshaft, this CS concept enables spatial separation of the mechanically robust and bioactive phases, providing a controlled design route to examine how changes in geometry and material distribution affect the scaffold's mechanical properties while maintaining regions of bioactive ceramic exposure.

The main objective of the study was to design scaffolds with mechanical and biological properties comparable to those of bone. To reach this objective, we formulated a printable ink containing Ti6Al4V powder, Ak powder, hydroxypropyl methylcellulose (HPMC), and a cellulose-derived polymer that served as a binder and stabilizer [23]. This ink formulation enabled the fabrication of stable, high-fidelity scaffolds. The mechanical performance of the scaffolds was evaluated *via* uniaxial compression testing to determine elastic modulus and compressive yield strength and observe failure behavior. In parallel, bioactivity was assessed by (i) immersing scaffold specimens in a revised simulated body fluid (r-SBF), to gain insights into their mineralization behavior under physiologically relevant conditions and (ii) assessing the viability and spatial organization of preosteoblast cells on the different scaffold designs.

2. Materials and methods

2.1. Materials and scaffold design

We designed porous scaffolds with varied material compositions of Ti6Al4V and Ak to optimize the mechanical properties while simultaneously enhancing osteo-induction [14]. The X-ray diffraction (XRD) pattern of the starting Ak material is shown in Figure S2 of the supplementary document. Two distinct scaffold architectures were developed (Fig. 1a). The first scaffold design featured 400 μm strut spacing, based on the finding that cell proliferation and bone in-growth occur most effectively in scaffolds with pore sizes between 400 and 500 μm [19]. The monolithic scaffolds with a diameter of 10 mm and a height of 10.5 mm were fabricated from the inks containing Ti6Al4V (Ti) and a composite composed of 90 wt%Ti6Al4V and 10 wt% Ak (TiAk), incorporating a 90°-layer shift between layers (Fig. 1a). The inclusion of alternating 0° and 90° struts was intended to improve the mechanical performance by promoting balanced load distribution and enhanced structural integrity. The second scaffold design was characterized by a core-shell (C-S) multi-material configuration, in which the core with a diameter of 5 mm and a height of 10.5 mm was made of the Ti6Al4V alloy and the shell with an outer diameter of 10 mm and a height of 10.5 mm was made of the TiAk composite or vice versa.

2.2. Ink preparation

Hydroxypropyl methylcellulose (HPMC), a water-soluble cellulose derivative, was used as a binder and rheology modifier to enhance ink stability. Two types of inks were prepared: one containing only Ti6Al4V powder and the other containing the composite consisting of 90 wt% Ti6Al4V powder and 10 wt% Ak powder, corresponding to the volume fractions of 87 vol% and 13 vol% for Ti6Al4V and Ak, respectively.

Binder solution: A 5.5 wt% HPMC binder solution was prepared by heating 150 mL distilled water to 80 °C. Once the temperature was

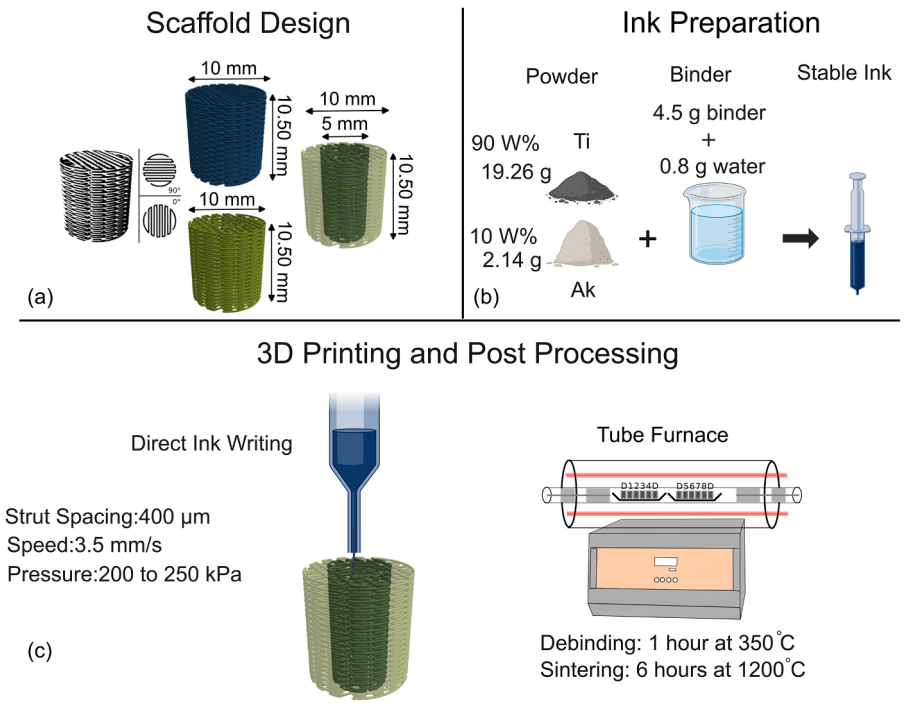

Fig. 1. An overview of the scaffold designs and fabrication workflow. (a) Schematic drawings of scaffold geometry, dimensions, and material compositions. (b) Ink preparation process, detailing the weight percentages of Ti6Al4V, akermanite, binder, and water. (c) 3D printing and sintering parameters, including extrusion settings and thermal profile used for debinding and sintering.

stabilized, 100 mL water was transferred to a beaker, and 5.8 *g* HPMC powder (H7509, Sigma-Aldrich, Germany) was gradually added under stirring at 500 RPM. At 70 °C, HPMC remained insoluble, allowing homogeneous dispersion. After 5 min, heating was terminated and the beaker was covered to prevent evaporation. Upon cooling, HPMC became dissolved, resulting in a solution with increased viscosity and without the need for continued stirring. The binder solution was then degassed prior to use.

Ti6Al4V ink: 21.4 *g* Ti6Al4V powder with 10–45 μm particle sizes and a spherical particle morphology, supplied by Advanced Powders and Coatings, Canada, was mixed with 4.5 *g* binder in a glass beaker to form a homogeneous ink. The mixture was transferred into a 10 mL syringe barrel and sealed with a piston. To ensure uniformity and remove air bubbles, the ink was extruded into a second syringe barrel prior to 3D printing.

Ti6Al4V-Ak ink: 19.26 *g* Ti6Al4V powder was mixed with 2.14 *g* Ak powder (having particle sizes >63 μm and an irregular morphology, supplied by Shanghai Institute of Ceramics, Chinese Academy of Sciences, China, 4.5 *g* binder, and 0.8 *g* distilled water to adjust viscosity (Fig. 1b). Manual stirring was applied until all the components became fully dispersed to form a homogeneous mixture, which was then transferred to a syringe barrel. The same as for the Ti6Al4V-containg ink, the composite-containing ink was extruded into a second barrel before use in 3D printing.

2.3. Scaffold fabrication

All the scaffolds were fabricated using a GeSiM Bioscaffolder 3.2 (GeSiM Bioinstruments and Microfluidics, Germany) equipped with a pneumatically activated extrusion system and a tapered nozzle with a diameter of 410 μm. The inks were loaded into single-use 10 mL Nordson EFD syringe barrels with a Luer lock connector to minimize cross-contamination between materials.

3D printing was conducted in a layer-by-layer fashion, allowing sufficient drying time between layers. Drying time, rather than machine kinematics, was the primary factor limiting the printing speed. A total of nine scaffolds were printed per build cycle. Key printing parameters included: print speed (3.5 mm/s), extrusion pressure (200–250 kPa), start delay (1 s), tear-off distance (5 mm), and tear-off speed (5 mm/s) (Fig. 1c). The infill density was 42% for the Ti and TiAk groups, and 40% for the C-S groups.

The as-printed scaffolds underwent debinding and sintering in a tube furnace (STF16/180, Carbolite Gero Ltd., UK). They were placed in alumina crucibles, shielded with titanium foil and surrounded by a sacrificial material to minimize any possible oxidation. An inert atmosphere was established by purging the furnace chamber with high-purity argon (>99.9%) for 2 h prior to heating.

Debinding was performed by heating the as-printed scaffolds to 350°C at a ramp rate of 2°C/min, holding at that temperature for 1 h to decompose the methylcellulose binder. This was followed by sintering at 1200°C for 6 h, using a ramp rate of 10°C/min, followed by furnace cooling under argon flow at rates exceeding 20°C/min (Fig. 1c). The chosen sintering temperature exceeded two-thirds of the melting point of Ti6Al4V (between 1604 and 1660°C), which was considered high enough to initiate atomic diffusion and neck formation between powder particles for densification. Notably, the applied sintering temperature (1200°C) is also below the melting point of akermanite (~1454°C) [24]. Studies on akermanite materials have shown that sintering at around 1200°C leads to significant densification and mechanical integrity in bulk ceramic samples without melting. For example, sintered akermanite tablets held at ~1200°C exhibit measurable strength and elastic modulus indicative of solid-state sintering consolidation [25]. While this high-temperature and extended-time sintering protocol promoted densification, it could inevitably have induced grain growth and reduced mechanical strength.

2.4. Material and structure characterization

X-ray diffractometry (XRD) analysis was performed on the sintered scaffolds to identify phase constituents, using a D8 Advance diffractometer (Bruker, Billerica, MA, USA) equipped with Bragg-Brentano geometry and Cu Kα radiation (λ = 1.5406 Å), operated at 45 kV and

45 mA. Scans were acquired over a 2θ range of 5 to 110°, with a step size of 0.04° and a counting time of 2 s per step. Phase identification was performed using the Bruker DiffracSuite.EVA software (version 6.1).

Surface morphology, strut geometry, and material interfaces were observed using a scanning microscope (SEM, JSM-IT100LA, JEOL, Japan), while elemental compositions were determined with an attached energy-dispersive X-ray spectroscopy (EDS). Specimens were mounted on a conductive double-sided carbon tape and cleaned with compressed air to remove loose particles. A thin gold layer was deposited using a sputter coater (Auto Fine Coater, JEOL JFC-1300, Japan) under vacuum (< 0.1 mbar) for 90 s to ensure conductivity and to prevent surface charging. SEM imaging was performed at magnifications between 30 and 800. EDS analysis was performed at a working distance of 10 mm and an accelerating voltage of 15 kV, using a beam current of 60 nA. Particular attention was paid to the interfaces between the materials in the multi-material scaffolds.

Micro-computed tomography (μCT) was performed on one representative specimen from each group using a ZEISS Xradia Context microCT (Dublin, CA, USA) to assess scaffold geometry and porosity. Specimens were scanned over 360° with an angular step of 0.12°, an isotropic voxel size of 5 μm, and scan parameter set at 150 kV and 100 μA. Each scan took approximately 26 min. Image segmentation was conducted using the Dragonfly software (version 2022.1.1249, Canada), employing the Otsu thresholding method for accurate binarization and phase separation [26].

Porosity was analyzed at both micro and macro levels (Table 1). Micro-porosity was defined as the pore volume within scaffold struts, normalized to the volume of a cylindrical region encompassing the scaffold. For the C-S structures, micro-porosity was also measured separately in the core and in the shell across the top, middle, and bottom regions, and calculated as pore volume normalized to the volume of the corresponding strut segment (core or shell). Reported values represent the average across these regions. Macroporosity included both micro-porosity and inter-strut voids.

To investigate the decomposition temperature of Ak in the presence of Ti, a powder mixture containing 4.50 g Ti and 0.50 g Ak powder was prepared and subjected to thermogravimetric analysis (TGA). TGA measurements were carried out using a PerkinElmer TGA 8000 instrument (PerkinElmer, USA) under a nitrogen atmosphere. An initial sample mass of 31.538 mg was equilibrated at 30°C for 1 min, followed by heating from 30 to 950°C at a constant rate of 20°C min^{-1}.

The phase composition of the TGA residue was determined by XRD using a Bruker D8 Advance diffractometer (Bruker, Germany) equipped with Cu-Kα radiation (λKα1 = 1.54060 Å, λKα2 = 1.54439 Å) and a Lynxeye-XE-T position-sensitive detector. Measurements were performed in Bragg–Brentano geometry over a 2θ range of 5–90° with a step size of 0.01° and a counting time of 0.2 s per step. The instrument was operated at 40 kV and 25 mA using a motorized variable-divergence slit of 10 mm.

Table 1
The comparison between the designed and as-built porosities of the 3D printed specimens measured from μCT imaging.

Specimen group	Porosity total (Macro porosity) μCT (%)	Micro porosity μCT (%)	Design porosity (%)	Material area on the cross section (mm^2)	Deviation from designed porosity (%)
Ti	55.86	1.33	58	28.47	−3.47
TiAk	50.38	1.44	58	33.76	−9.06
C-S Ti-TiAk	37.05	1.42	60	39.12	−24.37
C-S TiAk-Ti	34.85	1.25	60	40.60	−26.40

2.5. Mechanical testing

Mechanical properties of the fabricated scaffolds, including elastic modulus and yield strength, were evaluated through uniaxial quasi-static compression testing. Compression testing was performed using a universal testing machine (Z100, Zwick/Roell, Ulm, Germany) equipped with a 100 kN load cell, following ISO 13,314:2011 guidelines for porous metal structures [27]. A scaffold specimen was centrally positioned between two flat steel plates and compression was applied under displacement control. The testing parameters included a preload of 10 N, a crosshead speed of 0.05 mm/s, and a total displacement of 5 mm, corresponding to 50–55% compressive strain. After each test, debris was removed, and the largest remaining scaffold fragment was recovered for analysis. The elastic modulus was calculated as the maximum slope within the linear elastic region of the stress-strain curve. For all the specimens, the yield point was defined as the deviation of the stress–-strain curve from the initial linear elastic behavior.

2.6. Immersion tests

Immersion tests were performed in revised simulated body fluid (r-SBF) to evaluate scaffold bioactivity [28]. Specimens were incubated in a cell culture incubator under the following conditions: 37 ± 0.5°C, 5% CO_2, and 95% relative humidity. The solution volume-to-surface area ratio was maintained at 6.7 mL/cm^2 [13]. The apatite-forming ability of the scaffolds was assessed by immersion in r-SBF prepared according to Oyane et al. [29]. R-SBF was selected because it was designed to match the ion concentrations of human blood plasma, including Cl^- and HCO_3^-, whereas conventional SBF deviates particularly in these ions. Since bicarbonate and chloride levels influence the composition and structure of the apatite precipitated in SBF, the use of r-SBF provides a more physiologically relevant environment for assessing bone-like apatite formation on the scaffold surface.

Before testing, the specimens were sterilized by heating in an oven at 120°C for 2 h, and the r-SBF was filtered through a 0.4 μm membrane (Merck Millipore, Germany). After 7 days of immersion, scaffold surface morphology and elemental composition were analyzed using SEM and EDS (JEOL JSM-IT100, Japan). The concentrations of the ions (i.e., Ca^{2+}, P, Mg^{2+}, PO_4^{3-}, and Si) in the r-SBF were quantified after 7 days of immersion using inductively coupled plasma optical emission spectroscopy (ICP-OES, iCAP 6500 Duo, Thermo Scientific, USA).

2.7. Preculture of preosteoblasts and cytocompatibility tests

Preosteoblasts (MC3T3-E1, Sigma Aldrich, Germany) were precultured in the cell culture medium containing α-minimum essential medium (α-MEM, Thermo Fisher Scientific, USA) without ascorbic acid and supplemented with 10% fetal bovine serum (FBS, Thermo Fisher Scientific, USA) and 1% penicillin/streptomycin (p/s, Thermo Fisher Scientific, USA) for 7 days. The cells were incubated at 37°C in a humidified atmosphere with 5% CO_2 The culture medium was refreshed every 2 to 3 days.

For the cytocompatibility tests, the sterilized porous Ti6Al4V alloy, Ti6Al4V-Ak composite, and the core-shell specimens (duplicates for each group) were pre-immersed in culture medium for 4 h before cell seeding. Then, the cells (1×10^5 cells/specimen) were seeded on the porous specimens in 4 mL cell culture medium. After 4 days, the specimens were stained with calcein and ethidium homodimer-1 to determine the cell viability (Thermo Fisher Scientific, USA). The live and dead cells on the scaffolds were observed by fluorescence microscopy (ZOE cell imager, Bio-Rad, USA). Furthermore, SEM imaging of the specimens was performed to observe the cell spatial organization and the surface-cell interface. After 4 days of culture, the specimens were washed in PBS, fixed with 4% formaldehyde (Sigma Aldrich, Germany) for 20 min, followed by dehydration stages in 70 and 100% ethanol for 10 min each. The specimens were dried overnight prior to SEM imaging

on a JEOL JSM-IT100, Japan, at 15 kV accelerating voltage, 100x magnification and a 10 mm working distance.

2.8. Statistical analysis

Statistical analyses were carried out with IBM SPSS Statistics version 29.0.2.0 on the mechanical test data to assess the differences in elastic modulus and yield strength among scaffold groups. A one-way ANOVA was conducted to determine whether overall group differences existed. Because ANOVA only establishes that at least one difference is present without identifying which groups differ, Bonferroni-adjusted *post hoc* tests were performed for pairwise comparisons. The Bonferroni correction was selected to ensure strict control of the family-wise error rate (FWER) and thereby minimize the likelihood of false positives when interpreting group differences. All the statistical analyses were conducted at a 95% confidence level ($p < 0.05$).

3. Results and discussion

3.1. Quality of the fabricated scaffolds

The scaffolds fabricated *via* DIW closely matched the intended designs in their green (as-printed) state (Fig. 1a), with well-defined layer patterns and consistent layer heights. Minor deformation of the bottom layer, resulting from intentional compression against the glass build plate, was introduced to ensure adhesion during 3D printing and was considered a necessary aspect of the process.

It is important to note that batch-to-batch variability was observed across all the groups, with scaffold weights differing by more than 20% despite identical printing parameters used (Table 2). In contrast, variability within single batches was substantially lower. Contributing factors likely included inconsistencies in ink preparation, differential drying during mixing, and entrapped air bubbles. Improved control of ink flow rate and standardized nozzle tip usage may help reduce these inconsistencies.

Post-sintering analysis showed visible air pockets on the top surfaces of both Ti6Al4V and TiAk scaffolds (Fig. 2a,e, and *g*), likely caused by entrapped gases or incomplete densification. The Ti6Al4V scaffolds exhibited a higher degree of particle bonding (Fig. 2b) as compared to the TiAk composite (Fig. 2f and h), attributed to the presence of Ak. As a ceramic phase, Ak could have interfered with the sintering behavior of the Ti alloy powder and reduced interparticle cohesion.

Air inclusions were the most prevalent defect, originating during the mixing process when air became entrapped between powder particles and the liquid binder. While vacuum degassing or centrifugation can be used to eliminate entrapped air, these methods may introduce secondary issues such as water boiling or sedimentation of heavier particles. A more effective approach involves reducing ink viscosity and employing gentle agitation to maintain particle suspension while minimizing reintroduction of air bubbles [30].

Surface-level defects, including broken strands, minor sagging, coalescence, and occasional air pockets, were observed primarily at the external regions of the scaffolds (see Figure S1 of the supplementary document). These imperfections are characteristic of extrusion-based 3D printing and are often interrelated; efforts to mitigate one may inadvertently introduce others, underscoring the need for a balanced, process-wide optimization strategy. Importantly, no significant internal defects were identified that could compromise mechanical performance (see subSection 3.2 for qualitative and quantitative results).

Over extrusion (Figures S1a b and c of the supplementary document) and strand breakage (Figure S1d of the supplementary document) were frequently associated with mismatches between ink flow rate and printhead speed. Strand breakage can also result from entrapped air bubbles within the ink, which disrupt feedstock material continuity during extrusion. Calibrating the flow rate to match the motion of the printhead can significantly reduce these defects. However, pneumatically driven extrusion systems, such as the GeSiM Bioscaffolder, may still exhibit variability due to inherent limitations in pressure control.

Overall, effective defect mitigation in extrusion-based 3D printing requires precise tuning of multiple parameters, including ink rheology, flow rate, and mixing technique. Achieving consistent, defect-minimized prints demands an integrated approach that considers the complex trade-offs between material behavior, equipment constraints, and process stability.

Despite these imperfections, the 3D-printed scaffolds retained their overall structural integrity and macro-architecture. These results confirm the feasibility of using DIW for fabricating multi-material, porous scaffolds with adequate geometric fidelity.

Table 2
Statistical summary of scaffold weights after sintering showing within-batch variability, between-batch variation, and mass ranges (min–max).

Specimen group	Within-batch variability (%)	Between-batch variation (%)	Mean Mass (g)	Min Mass (g)	Max Mass (g)
Ti	1.36	29.1	1.15	0.983	1.318
TiAK	1.93	0.68	0.953	0.95	0.956
C-S Ti-TiAK	0.39	12.45	1.41	1.322	1.498
C-S TiAK-Ti	0.36	12.63	1.483	1.389	1.576

3.2. Morphologic characteristics of the fabricated scaffolds

μCT analysis revealed significant variations in both micro- and macro-porosity across the different scaffold designs (Fig. 3a,b,c,e,f and g). In the core-shell configurations, micro-porosity within the titanium alloy core, was 17.43% ±1.5%, while the surrounding TiAk shell exhibited a micro-porosity of 32.2% ± 0.53%. In the reverse configuration (i.e., with a TiAk core and a titanium alloy shell), the micro-porosity values were 35.3% ± 0.5% for the core and 17.4% ± 3.2% for the shell. Notably, greater shrinkage occurred in the titanium alloy regions of the C-S designs, suggesting material-specific densification behavior.

The designed porosity for the C-S scaffolds was approximately 60% for the entire structure. The observed reduction in porosity was consistent with the expected shrinkage of the titanium region only, as a result of particle bonding and densification during sintering at 1200°C for 6 h. The unique material configurations of the C–S scaffolds resulted in higher material-to-pore ratios compared with the monolithic Ti6Al4V and TiAk scaffolds (Table 1). μCT data confirmed increased material accumulation within the cross-sectional area of the C-S structures, particularly at the interface between the core and shell (Table 1). This is attributed to the consistent strut thickness that was maintained across intersecting layers, which promoted localized densification at the interface (Fig. 4a, b, e, and f). Consequently, these designs demonstrated greater material contents and reduced total porosities after sintering, directly contributing to their superior mechanical performance.

The differences between the designed and actual porosity values can primarily be attributed to densification during the sintering process. The titanium (Ti6Al4V) samples showed greater sinterability, as evidenced by the SEM images in Fig. 2 and the micro-CT porosity values, resulting in lower final porosity. In contrast, the TiAk composite exhibited reduced densification and higher porosity retention, which is consistent with the higher porosity values reported in Table 1.

Moreover, the DIW process may introduce heterogeneity in the initial porosity distribution due to variations in particle packing, binder removal, and localized shrinkage rates. These factors collectively contribute to the observed deviations between intended and measured porosity values (Figs. 3a, b, c, e, f,g, and 4a, b, c, e, f, g and Table 1).

3.3. Material characteristics

SEM of the sintered scaffolds showed distinct regions corresponding

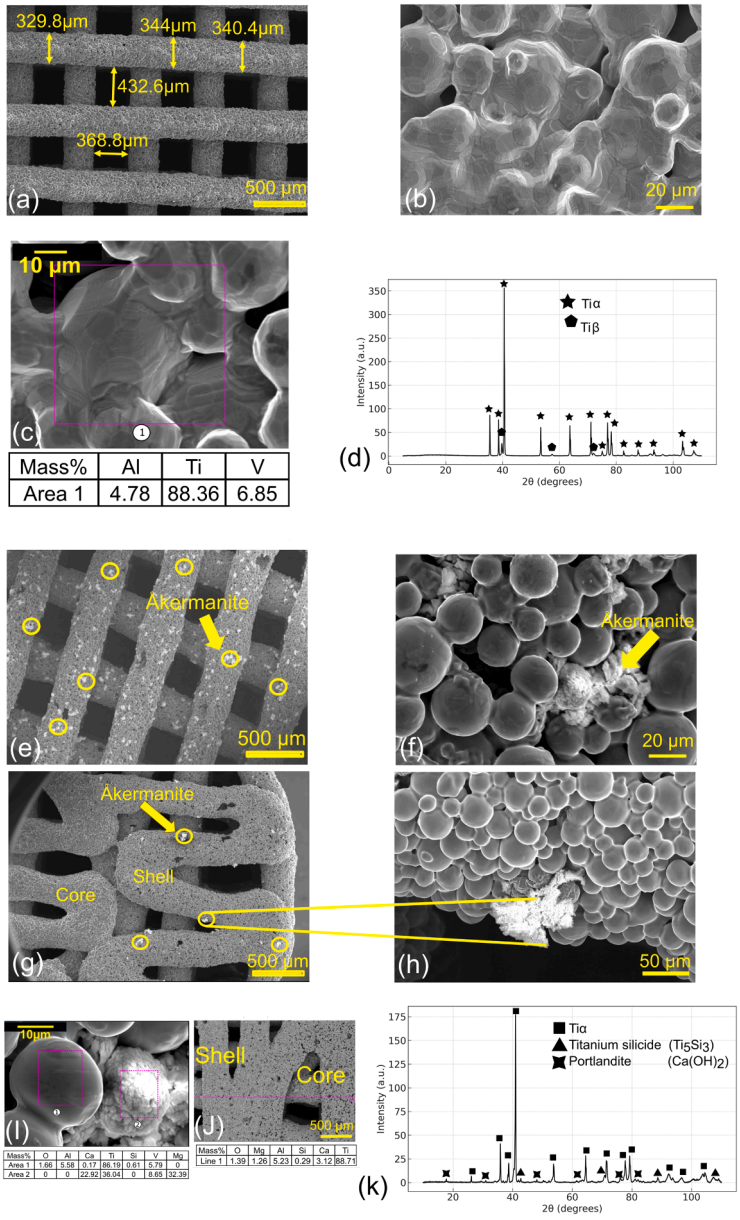

Fig. 2. Microstructural, elemental, and phase analysis of the sintered scaffolds. (a, b) SEM images of the Ti6Al4V scaffold at 40 × and 800 × magnifications, respectively. (c) EDS analysis of the Ti6Al4V scaffold after sintering. (d) XRD pattern of the Ti6Al4V scaffold showing phase constituents. (e, f) SEM images of the Ti6Al4V-akermanite composite scaffold at 40 × and 800 × magnifications, respectively, showing uniform dispersion of akermanite (the white spots). (g, h) SEM images of the core-shell scaffold (Ti6Al4V core and Ti6Al4V-akermanite shell) at 40 × and 400 × magnifications, respectively. (i) EDS analysis of the Ti6Al4V-akermanite composite scaffold. (j) EDS line analysis of the core-shell scaffold showing elemental distribution. (k) XRD analysis of the Ti6Al4V-akermanite composite scaffold, indicating phase evolution after sintering.

to the different material components. In the TiAk composite scaffolds, Ak particles appeared as bright spots uniformly dispersed on the titanium alloy matrix (Fig. 2e,f,*g* and h). Shrinkage mismatch between the core and shell could, in principle, lead to interfacial separation or cracking after sintering. However, we did not observe interfacial debonding or cracking in our samples. A cross-sectional SEM image of the core–shell interface will be added to demonstrate effective bonding and the absence of cracks (Figure S3 of the supplementary document).

EDS line and area analysis confirmed the presence and spatial distributions of calcium, silicon and magnesium, the key elements of Ak, indicating successful incorporation of the ceramic phase (Fig. 2i and j). EDS area analysis of a representative particle (denoted as region 2 in Fig. 2i) confirmed the presence of calcium and magnesium.

EDS area analysis of the Ti6Al4V scaffolds confirmed the presence and spatial distribution of aluminum, titanium, and vanadium (Fig. 2c). XRD analysis of the Ti6Al4V scaffolds identified two metallic phases: the α and β phase (Fig. 2d). These minor peaks are consistent with the known alloy microstructure of the Ti6Al4V system.

In contrast, XRD analysis of the sintered TiAk composite revealed significant phase transformation. Despite the reported thermal stability of single-phase Ak up to 1250 °C [31], no crystalline peaks of Ak were detected after sintering (Fig. 2k). Instead, secondary phases such as titanium silicide and portlandite ($Ca(OH)_2$) were identified. The presence of portlandite was unexpected, as it typically decomposes at temperatures well below the sintering temperature of 1200 °C [32], suggesting that its formation may have occurred during post-sintering exposure to ambient humidity. Moreover, no magnesium-containing crystalline phases were detected, implying that magnesium either volatilized or

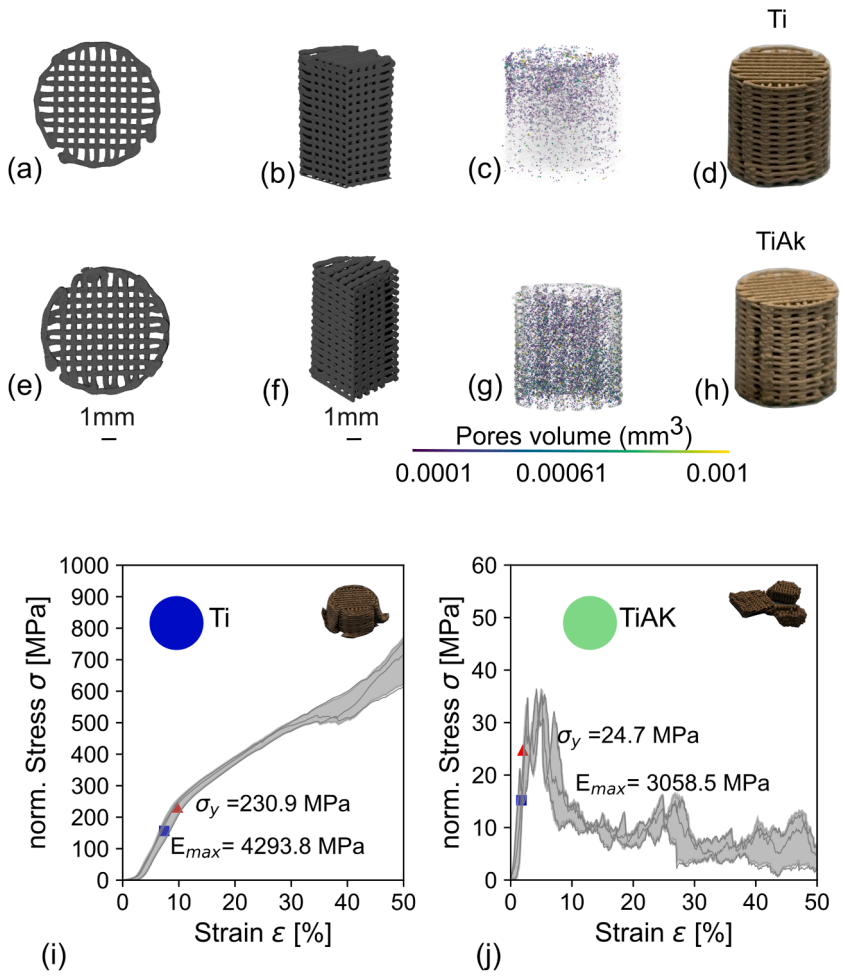

Fig. 3. μCT analysis (n = 1) and mechanical behavior (n = 3) of the sintered Ti6Al4V and Ti6Al4V-akermanite scaffolds under compressive loading. (a, b) μCT top view and sliced cross-section of the Ti6Al4V scaffold. (c) Pore volume distribution of the Ti6Al4V scaffold, ranging from 0.0001 to 0.001 mm^3. (d) Optical image of the sintered Ti6Al4V scaffold. (e, f) μCT top view and sliced cross-section of the Ti6Al4V-akermanite scaffold. (g) Pore volume distribution of the Ti6Al4V-akermanite scaffold, ranging from 0.0001 to 0.001 mm^3. (h) Optical image of the sintered Ti6Al4V-akermanite scaffold. (i, j) Relative-density-normalized compressive stress–strain curves for the Ti6Al4V and Ti6Al4V–akermanite scaffolds, respectively.

contributed to amorphous phase formation.

These results suggest that Ak must have undergone partial decomposition or/and chemical interactions during sintering, potentially influenced by the heating temperature and reactions with the titanium alloy [5]. This behavior highlights the importance of optimizing thermal processing parameters to preserve the ceramic phase and maintain the desired composite properties.

Thermogravimetric analysis of the Ti–Ak mixture under a nitrogen atmosphere, conducted from 30 to 950°C at a heating rate of 20°C min^{-1}, showed no decomposition-related mass loss. On the contrary, the sample mass increased from 31.543 mg to approximately 32.146 mg by the end of the run. Subsequent X-ray diffraction analysis identified akermanite ($Ca_2Mg(Si_2O_7)$) alongside Ti-based oxide phases, with akermanite remaining a major crystalline constituent of the sample (Figure S4a). These findings demonstrate that akermanite remains stable in contact with Ti up to 950°C, with no detectable sign of thermal decomposition within the resolution of the applied TGA and XRD methods (Figure S4b). Accordingly, the observed thermal changes in this temperature range are not consistent with akermanite breakdown, confirming its compatibility with Ti during heating up to 950°C.

3.4. Mechanical behavior

Compression testing showed two distinct mechanical responses corresponding to the scaffold compositions. The scaffolds composed of Ti6Al4V only displayed a typical mechanical behavior of a porous metallic material, characterized by an initial linear elastic region, followed by strain hardening and densification (Fig. 3i). In contrast, the TiAk composite scaffolds exhibited a more brittle behavior and collapsed at a low strain level, absorbing relatively little energy before complete failure (Fig. 3j).

The mechanical data were normalized by the relative density of each scaffold. Relative density was defined as the ratio of the measured scaffold bulk density to the theoretical density of the corresponding fully dense material. Bulk density was calculated from the measured mass and the external cylindrical volume of the scaffold, based on its measured diameter and height. For single-material scaffolds, the theoretical solid density was taken as that of the fully dense parent material. For composite and core-shell scaffolds, the theoretical solid density was determined by combining the densities of the constituent materials according to their composition or volume fractions (Table 3).

The C-S scaffolds exhibited significantly enhanced mechanical performance, compared to the monolithic Ti and TiAk scaffolds, with statistical analysis confirming the differences between the C-S TiAk-Ti *versus* Ti ($p = 0.005$), C-S TiAk-Ti *versus* TiAk ($p = 0.004$), C-S Ti-TiAk *versus* Ti ($p = 0.03$), and C-S Ti-TiAk *versus* TiAk ($p = 0.02$) (Figs. 3i,j, and 4i,j). The Ti6Al4V scaffolds showed an elastic modulus of 4.29 ± 0.177 GPa, while the TiAk composite scaffolds displayed the lowest

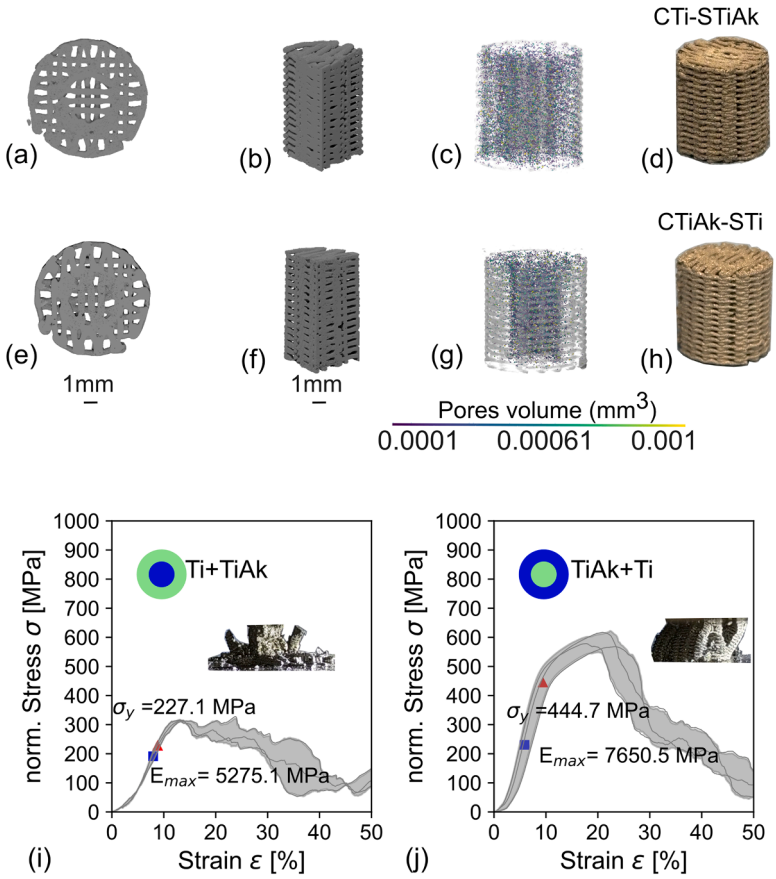

Fig. 4. μCT analysis (n = 1) and mechanical behavior (n = 3) of the sintered core-shell scaffolds under compressive loading. (a, b) μCT top view and sliced cross-section of the Ti-core/TiAk-shell scaffold. (c) Pore volume distribution of the Ti-core/TiAk-shell scaffold, ranging from 0.0001 to 0.001 mm³. (d) Optical image of the sintered Ti-core/TiAk-shell scaffold. (e, f) μCT top view and sliced cross-section of the TiAk-core/Ti-shell scaffold. (g) Pore volume distribution of the TiAk-core/Ti-shell scaffold, ranging from 0.0001 to 0.001 mm³. (h) Optical image of the sintered TiAk-core/Ti-shell scaffold. (i, j) Relative-density-normalized compressive stress–strain curves of the Ti-core/TiAk-shell and TiAk-core/Ti-shell scaffolds, respectively.

Table 3

Bulk density (ρ^*), solid density (ρ_s), and relative density ($\bar{\rho} = \rho^* / \rho_s$) of the Ti, TiAk, and core–shell scaffolds calculated from measured mass and cylindrical dimensions. For TiAk, $\rho_s$was estimated using a 90 wt% Ti-6Al-4 V / 10 wt% Ak rule-of-mixtures; for core–shell scaffolds, $\rho_s$was volume-weighted assuming a core diameter equal to half the cylinder diameter.

Sample	Bulk density ρ* (g/cm³)	Solid density ρs (g/cm³)	Relative density ρ*/ρs
Ti	1.41	4.43	0.32
TiAk	1.42	4.22	0.34
C-S Ti-TiAk	2.36	4.27	0.55
C-S TiAk-Ti	2.66	4.38	0.61

value of 3.05 ± 0.079 GPa. In contrast, the C-S configurations substantially increased elastic moduli to 5.27 ± 0.125 GPa for C-S Ti-TiAk and 7.65 ± 0.352 GPa for C-S TiAk-Ti, the latter achieving the highest among all the groups. These improvements are attributed to the synergistic interactions of the constituent materials and the optimized spatial distribution across the cross section, underscoring the importance of the core–shell architecture in enhancing mechanical performance.

In terms of yield strength, the C-S TiAk-Ti scaffolds again demonstrated the highest values, while the TiAk composite scaffolds recorded the lowest, consistent with the intrinsic brittleness of the ceramic component. The differences between the C-S TiAk-Ti and both Ti and TiAk ($p = 0.0001$ and $p = 0.0006$, respectively), as well as between Ti and TiAk, were all highly significant ($p = 0.0003$). See Figs. 4i, 4j, 3i and 3j.

Failure modes varied, depending on the core-shell arrangement. In the case of the C-S Ti-TiAk scaffolds, the brittle outer shell fractured earlier, initiating at approximately 5% strain and leading to unconfined failure between 15–20% strain (Fig. 4i). In contrast, the C-S TiAk-Ti configuration provided superior mechanical stability. The Ti6Al4V shell effectively confined the more brittle core, resulting in a nearly 1.9-fold increase in relative density normalized yield strength (from 227 MPa to 444 MPa). This arrangement also prevented material expulsion during failure, thereby preserving structural integrity under compressive loading (Fig. 4j).

While all the porous structures exhibited lower elastic moduli than the value of dense Ti6Al4V (typically around 114 GPa), primarily due to the designed and retained porosities, both the core-shell designs outperformed the monolithic scaffolds. Notably, the C-S TiAk–Ti scaffolds achieved the mechanical properties close to those of natural cortical bone (cortical bone typically having a compressive strength of 130–200 MPa and an elastic modulus of 7–30 GPa). Its elastic modulus lies near the lower end of that range under transverse loading, whereas its yield strength exceeds the upper physiological compressive strength under axial loading [33–35].

The brittleness of the TiAk composite scaffold, despite a relatively low Ak content (10 wt% corresponding to 13 vol%), indicates that ceramic inclusion compromises the mechanical performance instead of playing a reinforcing role. The TiAk scaffold exhibited a lower relative-density-normalized compressive yield strength and elastic modulus than the Ti scaffold, with the yield strength decreasing from 230.9 ± 1.74 to

24.7 ± 1.45 MPa and the elastic modulus from 4.29 ± 0.177 to 3.05 ± 0.079 GPa. (Fig. 3i and j). However, incorporating the Ti alloy as either the core or the shell could mitigate this limitation, significantly improving both strength and elastic modulus.

The mechanical properties of the core-shell scaffolds can be further tuned through adjustments in sintering condition, the core-shell cross-section area ratio, and pore geometry [36]. These parameters offer pathways for tailoring scaffold performance to meet specific clinical requirements.

From the results presented above, it is evident that scaffold architecture significantly influences the mechanical properties under compression. However, fabrication parameters such as sintering temperature, duration, and cooling rate also play a crucial role in determining final mechanical properties ([37,38]).

3.5. Interactions with the r-SBF

To perform a preliminary evaluation of scaffold bioactivity, the scaffolds of the four designs were immersed in r-SBF for 7 days. This initiated the nucleation of a calcium phosphate layer, which could subsequently develop into a hydroxyapatite layer on the Ak-containing scaffolds (Fig. 5a, b, and d). In contrast, the Ti6Al4V scaffolds showed minimal apatite deposition, indicating limited surface bioactivity (Fig. 5c).

Elemental analysis showed distinct compositional differences across the scaffold material configuration. The Ti6Al4V scaffolds were composed predominantly of Ti (97.59±1.54 wt%) and Al (2.41±1.54 wt %), with no detectable Ca or P, confirming their bioinert surface behavior (Fig. 5c). In contrast, the Ak-containing regions of the scaffolds showed clear signs of bioactivity, with the concentrations of Ca (6.71

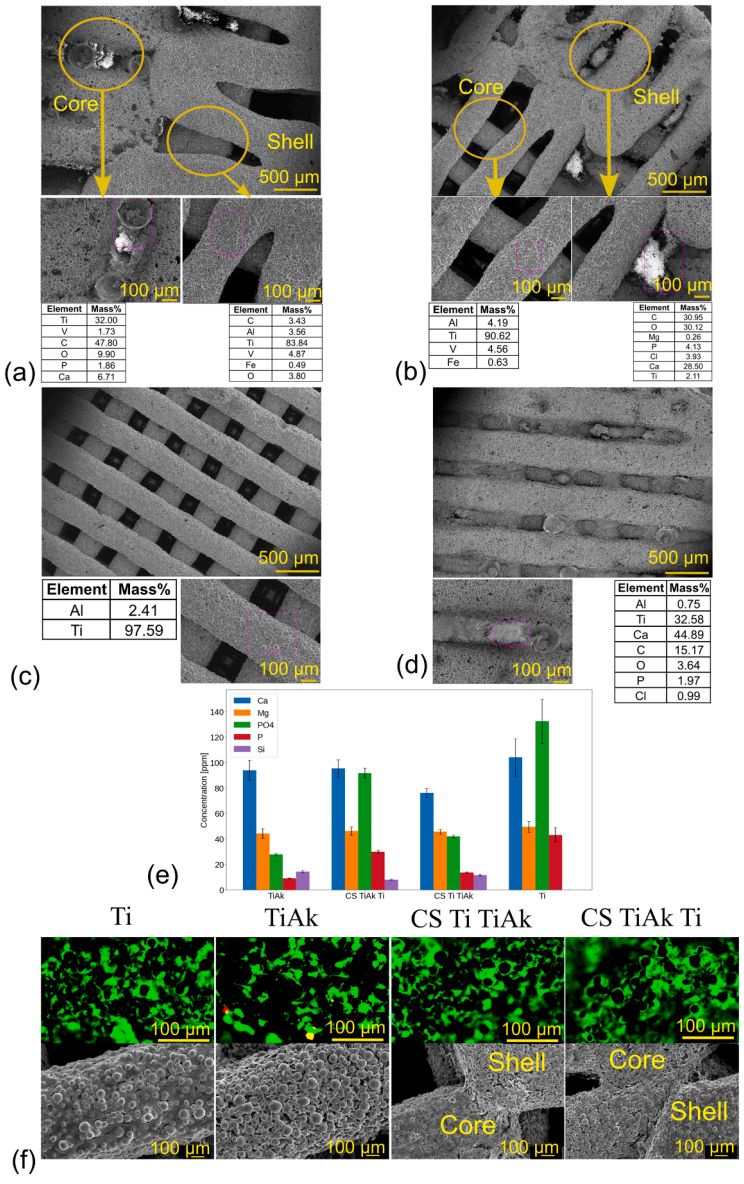

Fig. 5. Apatite formation on the scaffolds after 7-day immersion in the revised simulated body fluid (r-SBF) (n = 3). (a) SEM image of a TiAk-core/Ti-shell scaffold with EDS area analysis on both core and shell regions. (b) SEM image of a Ti-core/TiAk-shell scaffold with EDS area analysis on both regions. (c) SEM image and EDS area analysis of a monolithic Ti scaffold, showing minimal calcium and phosphorus presence. (d) SEM image and EDS area analysis of a monolithic TiAk scaffold, confirming calcium phosphate deposition. (e) The concentrations of soluble ions in the r-SBF solution. (f) Cytocompatibility and surface morphology of the Ti6Al4V and Ti6Al4V–akermanite scaffolds, (n = 2). Representative live/dead fluorescence images (top row, live cells in green and dead cells in red) and SEM micrographs (bottom row) of the Ti6Al4V, Ti6Al4V–akermanite and C-S scaffolds with Ti6Al4V core and Ti6Al4V–akermanite shell, and Ti6Al4V–akermanite core and Ti6Al4V shell.

±8.53 wt%) and P (1.86±2.648 wt%) (Fig. 5a). Ca:P ≈ 3, indicating a Ca-rich surface inconsistent with stoichiometric hydroxyapatite (Ca:P = 1.67). The Ca–P co-localization in selected regions suggests an early Ca-enriched stage that can precede apatite nucleation. A small amount of Mg (0.26±0.37 wt%) was also detected, which is known to enhance apatite crystallization and improve cellular responses [39]. (Fig. 5b).

In the core–shell scaffolds, apatite formation was primarily localized in regions where the Ak-derived Ca–Mg–Si-containing phase was present. EDS area analysis of the Ti (core)-TiAk (shell) scaffolds showed enriched Ca, P, and O in the outer shell, while the core remained dominated by Ti and Al (Fig. 5b). The detection of Cl (3.93±2 wt.%) suggests residual r-SBF components. These results confirm that Ak significantly enhances surface reactivity and promotes bioactive layer formation, in contrast to the inert Ti6Al4V regions (Fig. 5a, b, and d).

Collectively, these results indicate that the scaffolds incorporating Ak, particularly Ak in the shell, have a greater potential for osseointegration due to improved apatite formation, which is essential for bone cell attachment and mineralization. Further studies involving extended immersion durations, mechanical assessment of the apatite layer, and in vitro cellular assays are needed to validate long-term clinical viability.

A comparison of the ion-release profiles in rSBF further highlighted the effect of scaffold configuration on the bioactive ionic environment. The Ti scaffolds exhibited the highest Ca, PO4, and P concentrations (104.0 ± 14.7 ppm, 132.3 ± 17.3 ppm, and 43.2 ± 5.7 ppm, respectively). TiAk showed the highest Si release (14.33 ± 0.87 ppm) together with lower PO4 (27.87 ± 0.93 ppm) and P (9.07 ± 0.32 ppm). Among the core-shell designs, TiAk(core)-Ti(shell) exhibited higher Ca, PO4, and P concentrations (95.40 ± 6.86 ppm, 91.67 ± 3.84 ppm, and 29.90 ± 1.25 ppm, respectively) than Ti(core)-TiAk(shell) (76.07 ± 3.43 ppm, 41.90 ± 1.28 ppm, and 13.67 ± 0.42 ppm), indicating a stronger Ca/P-dominated ionic signature. In contrast, Ti(core)-TiAk(shell) showed higher Si release (11.57 ± 0.58 ppm) than TiAk(core)-Ti(shell) (7.93 ± 0.35 ppm), suggesting that exposing the Ak-rich phase at the surface promotes silicon delivery. The Mg concentrations were relatively similar across all groups, ranging from 44.20 ± 3.77 ppm to 49.43 ± 4.33 ppm, and should therefore be interpreted with caution. Since rSBF/SBF already contains Mg^{2+} as part of its baseline composition, the measured Mg values may partly reflect the immersion medium rather than true scaffold-derived release. Overall, these results indicate that Ak incorporation shifts the ionic profile toward measurable Si release, while TiAk at or near the scaffold surface appears more effective for generating a silicon-containing bioactive environment in rSBF.(Fig. 5e).

3.6. Cytocompatibility

Live/dead staining and the 4-day in vitro cell viability assay confirmed that all groups, including the portlandite-containing samples (Ti, TiAk, and both core–shell designs), were non-cytotoxic and supported viable preosteoblasts (Fig. 5f). SEM analysis, however, revealed differences in cell coverage: Ti surfaces showed confluent cell layers by day 4, whereas the TiAk group did not reach confluency, while both core–shell designs supported cell attachment, spreading, and a more uniform spatial distribution, particularly on the Ti regions. In parallel, although the initial akermanite phase decomposed/transformed during sintering, the Ak-derived regions exhibited enhanced in vitro surface bioactivity after 7 days in r-SBF, as indicated by bone-like apatite formation, Ca/P enrichment, and ion release. Together, these results show that phase transformation during sintering did not compromise cytocompatibility and that the intended Ca/Mg/Si-containing bioactive chemistry remained functionally effective in promoting apatite formation (Fig. 5).

Osteogenic activity of a material is mainly driven by its surface chemistry and topography, which regulate early protein adsorption and integrin-mediated adhesion, and by its ability to provide osteostimulatory cues such as ion release and apatite nucleation. Despite the non-cytotoxic level of ion concentrations measured [36], further studies are needed to understand the surface-induced effects of such core-shell scaffolds based on which the scaffolds can be further optimized for bone implants.

4. Conclusion

In this study, we successfully fabricated porous, multi-material scaffolds using the DIW technique and post-printing sintering. By incorporating Ak into Ti6Al4V and adopting a core-shell architecture, we achieved a balance between mechanical performance and bioactivity. The core-shell scaffolds exhibited higher relative-density-normalized elastic moduli (up to 7.65 ± 0.35 GPa) and yield strengths (up to 444 ± 8.1 MPa), outperforming the monolithic designs. In particular, the Ti6Al4V shell in the core-shell TiAk-Ti configuration effectively confined the brittle core, thereby improving structural integrity under compressive loading.

Given the high chemical affinity of titanium at elevated temperatures, reactions between Ti6Al4V and Ak can occur during sintering, and XRD confirmed that no crystalline akermanite remained in the sintered composites. In contrast, no decomposition of akermanite was observed in contact with Ti up to 950°C, as confirmed by TGA and XRD, indicating good thermal compatibility over the investigated temperature range. These findings suggest that akermanite decomposition in contact with Ti6Al4V may occur at temperatures between 950 and 1200°C, although further investigation is required to determine the exact decomposition temperature. Nevertheless, the Ak-derived Ca–Mg–Si-containing regions significantly enhanced bioactivity, as confirmed by apatite formation after immersion in r-SBF for 7 days. Elemental analysis showed increased Ca, P, and Mg contents in these regions, indicating enhanced apatite-forming ability and bone-bonding surface bioactivity, whereas Ti6Al4V remained bioinert.

These findings highlight the potential of DIW-fabricated core–shell scaffolds as customizable, load-bearing bone grafts with improved mechanical performance and enhanced surface bioactivity, as indicated by apatite formation in r-SBF, compared with monolithic Ti6Al4V scaffolds. The incorporation of the bioactive phase in spatially controlled regions provides a promising strategy for engineering mechanically robust scaffolds with bone-bonding surface characteristics, and merits further biological validation in future in vitro and in vivo studies.

Data availability

The data that support the findings of this study are available within this manuscript and its supplementary documents.

CRediT authorship contribution statement

S. Panahkhahi: Conceptualization, Data curation, Formal analysis, Funding acquisition, Investigation, Methodology, Project administration, Resources, Software, Supervision, Validation, Visualization, Writing – original draft, Writing – review & editing. **M.H. Zwart:** Data curation, Investigation, Methodology, Software, Validation. **V. Moosabeiki:** Data curation, Formal analysis, Software, Visualization. **L.B. Kunkels:** Writing – review & editing. **M.A. Leeflang:** Investigation, Resources, Writing – review & editing. **M. Klimopoulou:** Resources. **N. E. Putra:** Formal analysis, Investigation, Validation, Writing – review & editing. **L.E. Fratila-Apachitei:** Writing – review & editing. **J. Zhou:** Writing – review & editing. **M.J. Mirzaali:** Conceptualization, Methodology, Project administration, Resources, Supervision, Writing – review & editing. **A.A. Zadpoor:** Conceptualization, Methodology, Project administration, Resources, Supervision, Writing – review & editing.

Declaration of competing interest

The authors declare that they have no known competing financial

interests or personal relationships that could have appeared to influence the work reported in this paper.

Acknowledgments

The authors gratefully acknowledge Mr. Michel van den Brink (Department of Process and Energy) for conducting the ICP-OES measurements, Mr. Ruud Hendrikx (Department of Materials Science and Engineering) and Mrs. Xiaohui Liu (Department of Applied Sciences) for performing the XRD analysis, and Mrs. Aleksandra Kondakova (Department of Applied Sciences) for carrying out the TGA measurements. This publication is part of the project Biomimetic Design, Fabrication and Characterization of Hard-to-Soft Connections (project number 023.018.032), within the Promotiebeurs voor Leraren research programme awarded to Sara Panahkhahi, which is partly financed by the Dutch Research Council (NWO).

Supplementary materials

Supplementary material associated with this article can be found, in the online version, at doi:10.1016/j.mtla.2026.102748.

References

[1] F. Migliorini, G. La Padula, E. Torsiello, F. Spiezia, F. Oliva, N. Maffulli, Strategies for large bone defect reconstruction after trauma, infections or tumour excision: a comprehensive review of the literature, Eur. J. Med. Res. 26 (1) (2021), https://doi.org/10.1186/s40001-021-00593-9.

[2] K.A. Egol, A. Nauth, M. Lee, H.C. Pape, J. Tracy Watson, J. Borrelli, Bone grafting: sourcing, timing, strategies, and alternatives. Report, 2015. Available from, www.jorthotrauma.com.

[3] A. Oryan, S. Alidadi, A. Moshiri, N. Maffulli, Bone regenerative medicine: classic options, novel strategies, and future directions, J. Orthop. Surg. Res. (2014), https://doi.org/10.1186/1749-799X-9-18. PubMed PMID: 24628910.

[4] C. Kiernan, C. Knuth, E. Farrell, Endochondral ossification: Recapitulating bone development for bone defect repair, Developmental Biology and Musculoskeletal Tissue Engineering: Principles and Applications, 2018, pp. 125–148, https://doi.org/10.1016/B978-0-12-811467-4.00006-1.

[5] K. Marzban, S.M. Rabiee, E. Zabihi, S. Bagherifard, Nanostructured akermanite glass-ceramic coating on Ti6Al4V for orthopedic applications, J. Appl. Biomater. Funct. Mater. 17 (2) (2019), https://doi.org/10.1177/2280800018793819. PubMed PMID: 30139276.

[6] E. Marin, A. Lanzutti, Biomedical applications of titanium alloys: a comprehensive Review, Materials, (Basel) 17 (1) (2024) 114, https://doi.org/10.3390/ma17010114.

[7] Y.H. Kim, M. Choi, J.W. Kim, Are titanium implants actually safe for magnetic resonance imaging examinations? Archives of Plastic Surgery, Korean Soc. Plastic Reconstruct. Surg. (2019) 96–97, https://doi.org/10.5999/aps.2018.01466.

[8] J.L. Ong, D.L. Carnes, K. Bessho, Evaluation of titanium plasma-sprayed and plasma-sprayed hydroxyapatite implants in vivo, Biomaterials 25 (19) (2004) 4601–4606, https://doi.org/10.1016/j.biomaterials.2003.11.053. PubMed PMID: 15120505.

[9] S. Moon, S. Lee, I. Park, M. Lee, Y. Soh, T. Bae, et al., Bioactivity of Ti-6Al-4V alloy implants treated with ibandronate after the formation of the nanotube TiO $_2$ layer, J. Biomed. Mater. Res. B Appl. Biomater. 100B (8) (2012) 2053–2059, https://doi.org/10.1002/jbm.b.32769.

[10] K.A. Kravanja, M. Finšgar, A review of techniques for the application of bioactive coatings on metal-based implants to achieve controlled release of active ingredients. Materials and Design, Elsevier Ltd, 2022, https://doi.org/10.1016/j.matdes.2022.110653.

[11] G.S. Kaliaraj, T. Siva, A. Ramadoss, Surface functionalized bioceramics coated on metallic implants for biomedical and anticorrosion performance – a review, J. Mater. Chem. B 9 (46) (2021) 9433–9460, https://doi.org/10.1039/D1TB01301G.

[12] G. Balasubramani, Optimizing bone-metal implant interfaces: the role of bioceramic coatings in improving stability and tissue metabolism, Front. Mater. 11 (2024) 1–12, https://doi.org/10.3389/fmats.2024.1514559.

[13] N.E. Putra, K.G.N. Borg, P.J. Diaz-Payno, M.A. Leeflang, M. Klimopoulou, P. Taheri, et al., Additive manufacturing of bioactive and biodegradable porous iron-akermanite composites for bone regeneration, Acta Biomater. 148 (2022) 355–373, https://doi.org/10.1016/j.actbio.2022.06.009. PubMed PMID: 35690326.

[14] L. Xia, Z. Yin, L. Mao, X. Wang, J. Liu, X. Jiang, et al., Akermanite bioceramics promote osteogenesis, angiogenesis and suppress osteoclastogenesis for osteoporotic bone regeneration, Sci. Rep. 6 (2016) 1–17, https://doi.org/10.1038/srep22005.

[15] F. Baino, E. Fiume, Mechanical characterization of 45S5 bioactive glass-derived scaffolds, Mater. Lett. 245 (2019) 14–17, https://doi.org/10.1016/j.matlet.2019.02.086.

[16] P. Feng, C. Gao, C. Shuai, S. Peng, Toughening and strengthening mechanisms of porous akermanite scaffolds reinforced with nano-titania, RSC. Adv. 5 (5) (2015) 3498–3507, https://doi.org/10.1039/C4RA12095G.

[17] N.E. Putra, M.J. Mirzaali, I. Apachitei, J. Zhou, A.A. Zadpoor, Multi-material additive manufacturing technologies for Ti-, Mg-, and Fe-based biomaterials for bone substitution, Acta Biomaterialia. Acta Materialia Inc. (2020) 1–20, https://doi.org/10.1016/j.actbio.2020.03.037. PubMed PMID: 32268239.

[18] H. Chen, Q. Han, C. Wang, Y. Liu, B. Chen, J. Wang, Porous scaffold design for additive manufacturing in orthopedics: a review, Front. Bioeng. Biotechnol. Front. Media S.A.8 (2020) 609, https://doi.org/10.3389/fbioe.2020.00609.

[19] F. Deng, L. Liu, Z. Li, J. Liu, 3D printed Ti6Al4V bone scaffolds with different pore structure effects on bone ingrowth, J. Biol. Eng. 15 (1) (2021), https://doi.org/10.1186/s13036-021-00255-8.

[20] N. Abbasi, S. Hamlet, R.M. Love, N.T. Nguyen, Porous scaffolds for bone regeneration, J. Sci.: Adv. Mater. Devi. (2020) 1–9, https://doi.org/10.1016/j.jsamd.2020.01.007.

[21] F. Liu, Z. Mao, P. Zhang, D.Z. Zhang, J. Jiang, Z. Ma, Functionally graded porous scaffolds in multiple patterns: new design method, physical and mechanical properties, Mater. Des. 160 (2018) 849–860, https://doi.org/10.1016/j.matdes.2018.09.053.

[22] L.J. Gibson, et al., Cellular Solids: Structure and Properties, 4, Cambridge Univ. Press, Cambridge, 1990, pp. 93–123, ch.

[23] R.A. Vlad, A. Pintea, C. Pintea, E.M. Rédai, P. Antonoaea, M. Bîrsan, et al., Hydroxypropyl Methylcellulose—a key excipient in pharmaceutical drug delivery systems, Pharmaceutics 17 (6) (2025) 1–30, https://doi.org/10.3390/pharmaceutics17060784.

[24] A.L. Pereira, J.A. Morales Pereira, W.V. Bielefeldt, A.C Faria Vilela, Thermodynamic evaluation of viscosity behavior for CaO–SiO2–Al2O3–MgO slag systems examined at the temperatures range from 1500 to 1700°C, Sci. Rep. 13 (1) (2023), https://doi.org/10.1038/s41598-023-41404-x. PubMed PMID: 37770486.

[25] A.K. Sharafabadi, M. Abdellahi, A. Kazemi, A. Khandan, N. Ozada, A novel and economical route for synthesizing akermanite (Ca2MgSi2O7) nano-bioceramic, Mater. Sci. Eng. C 71 (2017) 1072–1078, https://doi.org/10.1016/j.msec.2016.11.021. PubMed PMID: 27987661.

[26] N. Otsu, A threshold selection method from gray-level histograms, IEEE Trans. Syst. Man Cybern. 9 (1) (1979) 62–66.

[27] ISO, ISO 13314:2011 - Mechanical testing of metals — Ductility testing — compression test for porous and cellular metals. Report, 2011.

[28] L. Yang, E. Zhang, Biocorrosion behavior of magnesium alloy in different simulated fluids for biomedical application, Mater. Sci. Eng. C 29 (5) (2009) 1691–1696, https://doi.org/10.1016/j.msec.2009.01.014.

[29] A. Oyane, H.M. Kim, T. Furuya, T. Kokubo, T. Miyazaki, T. Nakamura, Preparation and assessment of revised simulated body fluids, J. Biomed. Mater. Res. 65 (2) (2003) 188–195, https://doi.org/10.1002/jbm.a.10482. PubMed PMID: 12734811.

[30] N.E. Putra, M.A. Leeflang, M. Klimopoulou, J. Dong, P. Taheri, Z. Huan, et al., Extrusion-based 3D printing of biodegradable, osteogenic, paramagnetic, and porous FeMn-akermanite bone substitutes, Acta Biomater. 162 (2023) 182–198, https://doi.org/10.1016/j.actbio.2023.03.033. PubMed PMID: 36972809.

[31] H. Mohammadi, et al., Microstructure evolution, grain growth kinetics and mechanical properties of $Ca_2MgSi_2O_7$ bioceramics sintered at various temperatures, 4th ed., 15, Process. Appl. Ceram, 2021, pp. 357–365.

[32] Mikhail RSh, S. Brunauer, LE. Copeland, KINETICS OF THE THERMAL DECOMPOSITION OF CALCIUM HYDROXIDE, JOURNAL OF GOLLOID AND INTI~RFACE SCIENCE (1966). Report.

[33] E.F. Morgan, G.U. Unnikrishnan, A.I. Hussein, Bone Mechanical Properties in Healthy and Diseased States, Annu Rev. Biomed. Eng. (2018) 119–143, https://doi.org/10.1146/annurev-bioeng-062117-121139. PubMed PMID: 29865872.

[34] M.J. Mirzaali, J.J. Schwiedrzik, S. Thaiwichai, J.P. Best, J. Michler, P.K. Zysset, et al., Mechanical properties of cortical bone and their relationships with age, gender, composition and microindentation properties in the elderly, Bone 93 (2016) 196–211, https://doi.org/10.1016/j.bone.2015.11.018. PubMed PMID: 26656135.

[35] L.C. Gerhardt, A.R. Boccaccini, Bioactive glass and glass-ceramic scaffolds for bone tissue engineering, Materials. (Basel) 3 (7) (2010) 3867–3910, https://doi.org/10.3390/ma3073867.

[36] Z. Miri, H.J. Haugen, D. Loca, F. Rossi, G. Perale, A. Moghanian, et al., Review on the strategies to improve the mechanical strength of highly porous bone bioceramic scaffolds, J. Eur. Ceram. Soc. (2024) 23–42, https://doi.org/10.1016/j.jeurceramsoc.2023.09.003.

[37] Bandala E., Raymond L., Mitchell K., Rubbi F., Thella J., Osho B.O., et al. Distance-controlled direct ink writing of titanium alloy with enhanced shape diversity and controllable porosity. npj advanced manufacturing. 2025;2(1):4 doi:10.1038/s44334-025-00016-1.

[38] M. Dziaduszewska, A. Zieliński, Structural and material determinants influencing the behavior of porous Ti and its alloys made by additive manufacturing techniques for biomedical applications, Mater.. MDPI AG; (2021) 1–48, https://doi.org/10.3390/ma14040712.

[39] R. Zhao, X. Meng, Z. Pan, Y. Li, H. Qian, X. Zhu, et al., Advancements in nanohydroxyapatite: synthesis, biomedical applications and composite developments, Regen. Biomater. (2025), https://doi.org/10.1093/rb/rbae129.